

# Beta Tantalum Transmon Qubits with Quality Factors Approaching 10 Million

Atharv Joshi Apoorv Jindal Paal H. Prestegard Faranak Bahrami Elizabeth Hedrick Matthew P. Bland Tunmay Gerg Guangming Cheng Nan Yao Robert J. Cava Andrew A. Houck Nathalie P. de Leon\*

Atharv Joshi, Dr. Apoorv Jindal, Paal H. Prestegard, Dr. Faranak Bahrami, Elizabeth Hedrick, Matthew P. Bland, Tunmay Gerg<sup>1</sup>, Prof. Andrew A. Houck, Prof. Nathalie P. de Leon  
Princeton University, Department of Electrical and Computer Engineering, Princeton, NJ 08544, USA  
Email Address: npdeleon@princeton.edu

Guangming Cheng, Nan Yao  
Princeton University, Princeton Materials Institute, Princeton, NJ 08544, USA

Robert J. Cava  
Princeton University, Department of Chemistry, Princeton, NJ 08544, USA

Keywords: *Beta tantalum, tantalum, superconducting qubits, superconducting circuits, transmon, TLS loss, kinetic inductance*

Tantalum-based transmon qubits are a promising platform for building large-scale quantum processors. So far, these qubits have been made from tantalum films grown exclusively in the alpha phase ( $\alpha$ -Ta). The beta phase of tantalum ( $\beta$ -Ta) readily nucleates at room temperature, making it attractive for scalable qubit fabrication. However,  $\beta$ -Ta is widely believed to be detrimental to qubit performance because it has a lower superconducting critical temperature than  $\alpha$ -Ta. We challenge this prevailing belief by fabricating low-loss transmon qubits from  $\beta$ -Ta films on sapphire. Across 11 qubits, the mean time-averaged quality factor is  $(5.6 \pm 2.3) \times 10^6$ , with the best qubit recording a time-averaged quality factor of  $(10.1 \pm 1.3) \times 10^6$ . Resonator studies demonstrate that the dominant microwave loss channel is surface two-level systems, with the surface loss contribution for  $\beta$ -Ta being about twice that of  $\alpha$ -Ta.  $\beta$ -Ta films exhibit significant kinetic inductance, consistent with an estimated magnetic penetration depth of  $(1.78 \pm 0.02) \mu\text{m}$ . This work establishes  $\beta$ -Ta on sapphire as a material platform for realizing low-loss transmon qubits and other superconducting devices such as compact resonators, kinetic inductance detectors, and quasiparticle traps.

arXiv:2603.13174v1 [quant-ph] 13 Mar 2026

---

<sup>1</sup>Present address: Yale University, Departments of Applied Physics and Physics, New Haven, CT 06511, USA.

Superconducting qubits are a leading platform for building large-scale quantum processors, having achieved early milestones in quantum error correction [1, 2, 3, 4] and quantum simulation of many-body systems [5, 6, 7, 8]. Advancing the scale and performance of superconducting quantum processors requires understanding and eliminating material-related microwave losses in the constituent qubits [9]. Systematic improvements in material selection and device fabrication have recently led to sustained gains in the lifetimes and coherence times of superconducting qubits. Lifetimes exceeding 100  $\mu\text{s}$  have been realized in several material platforms [10, 11, 12, 13], with tantalum (Ta)-based 2D transmon qubits [10] and quantum memories [14] achieving millisecond-scale coherence.

State-of-the-art Ta superconducting qubits have thus far been made exclusively from films sputtered in the body-centered cubic (b.c.c.) phase ( $\alpha$ -Ta) [10, 15, 16, 17, 18]. While Ta thin films nucleate more readily at room temperature in the metastable tetragonal phase ( $\beta$ -Ta) [19],  $\beta$ -Ta is considered to be detrimental to qubit performance because it has a lower superconducting critical temperature ( $T_c$ ) than  $\alpha$ -Ta (Table 1). Superconducting qubits typically operate at few-photon powers and millikelvin temperatures. At these temperatures, we expect negligible microwave losses due to quasiparticles (QP) in thermal equilibrium, even with the low  $T_c$  of  $\beta$ -Ta. Assuming an equilibrium temperature of 20 mK, BCS theory predicts the fraction of Cooper pairs dissociated into QPs in a superconductor with  $T_c = 0.5$  K to be less than  $10^{-19}$  [20]. In practice, the observed fraction of dissociated Cooper pairs is several orders of magnitude larger ( $10^{-9} - 10^{-5}$ ), which implies that QP-induced losses in superconducting qubits primarily arise from non-equilibrium QPs [20]. However, in the qubit operating regime, microwave losses in many materials, including  $\alpha$ -Ta, are dominated by defects known as two-level systems (TLS), and not by QPs [21, 22, 23].

Experimental reports comparing microwave losses in  $\alpha$ -Ta and  $\beta$ -Ta are scarce and inconsistent. Measurements on  $\alpha$ -Ta resonators reveal TLS loss contributions from both the surface and bulk dielectrics [23]. Surface TLSs primarily reside in the native oxide, which predominantly consists of tantalum pentoxide ( $\text{Ta}_2\text{O}_5$ ) [24, 25]. The native oxide of  $\beta$ -Ta is similarly composed of  $\text{Ta}_2\text{O}_5$  [26]. Despite this similarity, three studies find an order-of-magnitude higher loss with weak power dependence in  $\beta$ -Ta resonators, indicating a non-TLS origin [27, 28, 29]. In contrast, two studies find comparable power-dependent losses in the presence of minority [30] or majority [31]  $\beta$  phase in mixed  $\alpha$ - $\beta$ -Ta resonators. A natural question is whether the microwave loss channels in  $\beta$ -Ta superconducting devices differ from those in  $\alpha$ -Ta.

Here, we fabricate superconducting resonators and transmon qubits from  $\beta$ -Ta films deposited on sapphire at room temperature. We measure shifts in resonator frequencies that are consistent with a large kinetic inductance contribution, and we quantify the sheet kinetic inductance ( $L_{k/\square}$ ) of the films to ensure reliable device design. We study the power and temperature dependence of the resonator internal quality factor ( $Q_{\text{int}}$ ), and show that microwave losses at few-photon powers and millikelvin temperatures are dominated by TLSs. We find that the TLS loss scales linearly with the resonator surface participation ratio (SPR) [32], indicating that the dominant loss channel is surface TLSs, and we quantify the apparent surface losses in  $\beta$ -Ta to be around two times higher than in  $\alpha$ -Ta [23]. Transmon qubits fabricated from  $\beta$ -Ta films exhibit relaxation times ( $T_1$ ) that are in line with the loss limit imposed by surface TLSs. The best qubit, with a frequency ( $f_q$ ) of 2.74 GHz, has a time-averaged relaxation time ( $\overline{T}_1$ ) of  $(585 \pm 75)$   $\mu\text{s}$ , which corresponds to a time-averaged quality factor ( $\overline{Q} = 2\pi f_q \overline{T}_1$ ) of  $(10.1 \pm 1.3) \times 10^6$ , over 85 hours of continuous measurement. The mean time-averaged quality factor across 11 qubits is  $(5.6 \pm 2.3) \times 10^6$ , a performance that is comparable to that of the best aluminum (Al) [12], niobium (Nb) [13, 33, 34, 35], and  $\alpha$ -Ta on sapphire [16] transmons. Our results establish  $\beta$ -Ta on sapphire as a material platform for realizing low-loss transmon qubits.

**Table 1:** Salient material properties of sputtered Ta [19, 36, 37, 38].

Phase	Crystal structure	Lattice parameters ( $\text{\AA}$ )	$T_c$ (K)	$\rho_n$ ( $\mu\Omega$ cm)
$\alpha$ -Ta	b.c.c.	$a = 3.3 - 3.4$	4.2 - 4.4	1 - 50
$\beta$ -Ta	tetragonal	$a = 5.3, c = 9.9 - 10$	0.5 - 1.0	150 - 220

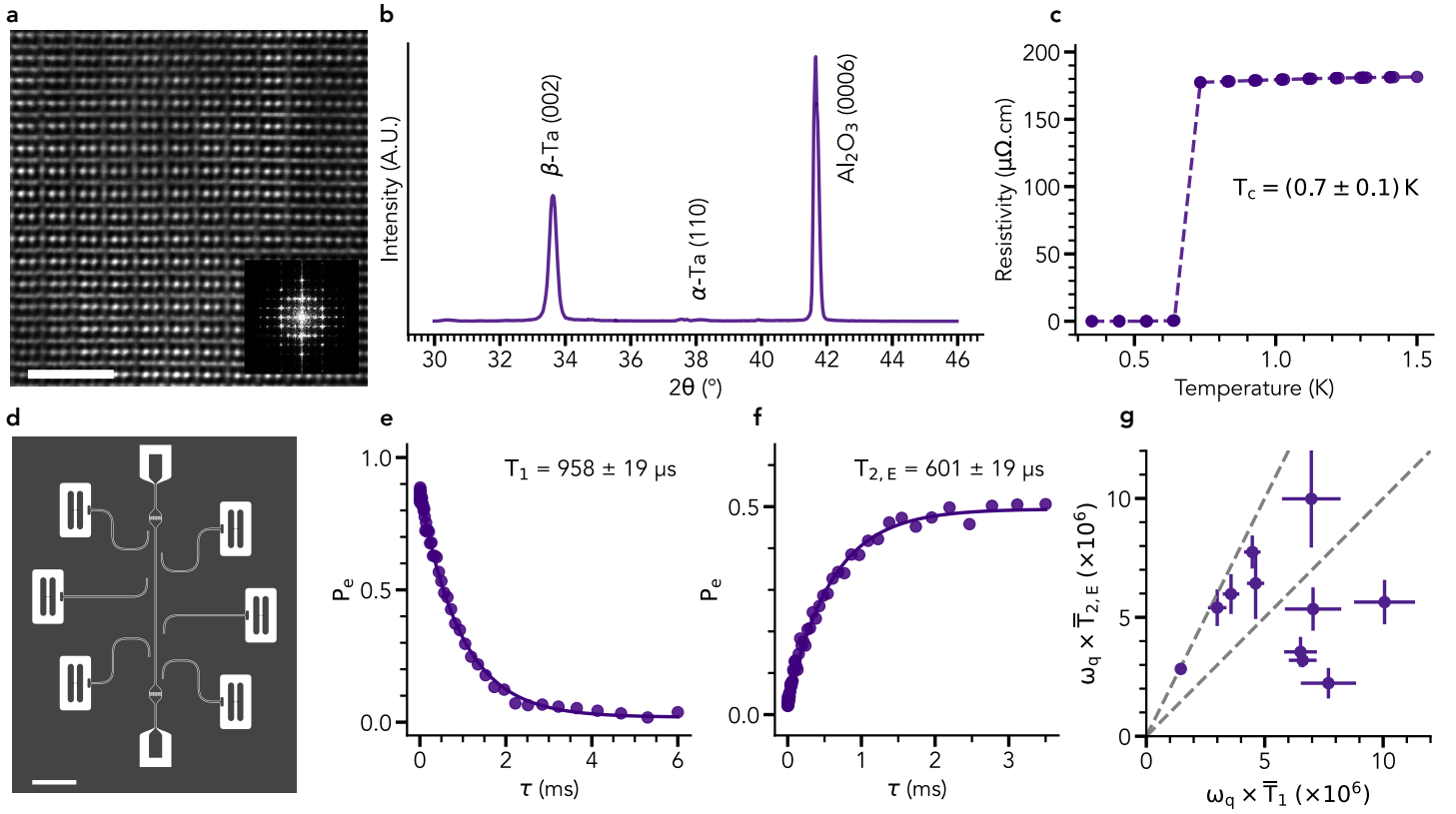


**Figure 1:  $\beta$ -Ta transmon qubits with quality factors approaching ten million.** (a) Cross-sectional STEM image of a Ta film on sapphire. Scale bar: 2 nm. Inset: Local area diffraction pattern identifies (001) as the preferred growth plane. (b) XRD pattern obtained from the Ta film shows intense peaks at  $33.6^\circ$  and  $41.7^\circ$  corresponding to  $\beta$ -Ta (002) [39] and  $\text{Al}_2\text{O}_3$  (0006) respectively, along with traces of  $\alpha$ -Ta (110). (c) Four-probe DC resistivity measurement across the superconducting transition of the Ta film. The  $T_c$  of  $(0.7 \pm 0.1)$  K is reported as the midpoint of the temperatures of the two consecutive data points that bracket the superconducting transition, and the uncertainty in  $T_c$  represents the measurement temperature step size. The dashed line is a guide to the eye. (d) Schematic of a chip with 6 transmon qubits on a sapphire substrate (white), where the transmon capacitor pads and ground plane are made from  $\beta$ -Ta (gray). Scale bar: 1 mm. Excited state population ( $P_e$ ) as a function of delay time ( $\tau$ ) for a qubit with  $f_q = 2.74$  GHz in a (e)  $T_1$  experiment showing a maximum  $T_1 = (958 \pm 19)$   $\mu\text{s}$  and (f)  $T_{2,E}$  experiment showing a maximum  $T_{2,E} = (601 \pm 19)$   $\mu\text{s}$ . Solid lines are fits to the data points and uncertainties in  $T_1$  and  $T_{2,E}$  represent the standard error (s.e.) estimated from the covariance matrix of the fit. (g) Plot of  $\bar{T}_1$  and  $\bar{T}_{2,E}$  multiplied by  $\omega_q = 2\pi f_q$  for 11 qubits, where error bars represent the standard deviation (s.d.) of the  $T_1$  and  $T_{2,E}$  time series. The two dashed lines, in ascending order of slope, depict the  $\bar{T}_{2,E} = \bar{T}_1$  and  $\bar{T}_{2,E} = 2\bar{T}_1$  limits respectively.

Unlike  $\alpha$ -Ta thin films, which require stringent growth conditions [15, 17, 18, 39, 40, 41, 42], such as elevated temperatures or seed layers,  $\beta$ -Ta films can be readily grown at room temperature [19, 36]. We deposit Ta films on 500  $\mu\text{m}$ -thick c-plane sapphire substrates at room temperature by DC magnetron sputtering (Section S1, Supporting Information). Cross-sectional scanning transmission electron microscopy (STEM) reveals a tetragonal unit cell with lattice parameters  $a = 5.3$   $\text{\AA}$  and  $c = 10$   $\text{\AA}$  (Figure 1a), which is characteristic of  $\beta$ -Ta (Table 1). X-ray diffraction (XRD) confirms the predominant crystallographic phase to be  $\beta$ -Ta (Figure 1b). A four-probe DC resistivity measurement as a function of temperature shows a  $T_c$  of  $(0.7 \pm 0.1)$  K and a normal state resistivity ( $\rho_n$ ) of  $(180 \pm 1)$   $\mu\Omega$  cm (Figure 1c), which agree with the reported values for  $\beta$ -Ta (Table 1). We pattern the  $\beta$ -Ta films into resonators and qubit wiring layers (Figure 1d) using photolithography and reactive ion etching (Section S2, Supporting Information). We fabricate Al/aluminum oxide/Al Josephson junctions for the qubits in an ultrahigh-vacuum electron-beam evaporation system, following procedures described in Reference [10]. All devices are measured in dilution refrigerators with base temperatures of 10 – 15 mK (Section S3, Supporting Information).

Despite the low  $T_c$  of the  $\beta$ -Ta films, transmon qubits with  $\beta$ -Ta capacitor pads show remarkably long relaxation and coherence times. The best qubit records a maximum  $T_1$  of  $(958 \pm 19)$   $\mu\text{s}$  (Figure 1e), Hahn

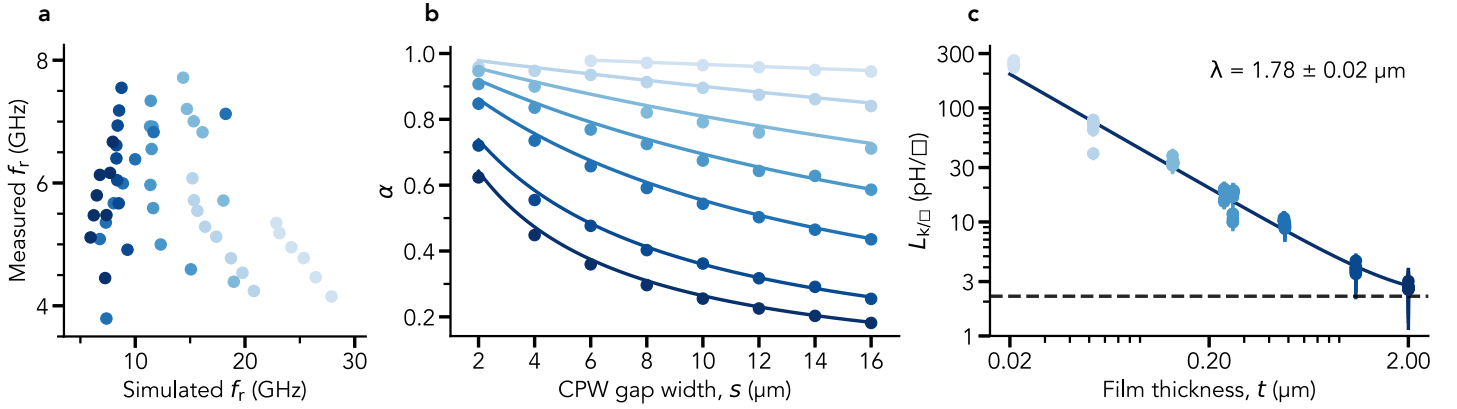


**Figure 2: Quantifying the kinetic inductance of  $\beta$ -Ta films.** (a) Scatter plot of measured and simulated resonance frequencies ( $f_r$ ) of 80 CPW resonators fabricated from 11  $\beta$ -Ta films with different thicknesses. Film thickness ( $t$ ) ranges from 0.02  $\mu\text{m}$  (lightest blue) to 2.00  $\mu\text{m}$  (darkest blue) and roughly doubles with each intermediate shade of blue. The measured  $f_r$  is always lower than the simulated  $f_r$ , with the largest shifts to lower frequencies occurring in the thinnest films. (b) Plot of the kinetic inductance fraction ( $\alpha$ ) versus CPW gap width ( $s$ ) for a subset of 7 films. We use electromagnetic simulations (Section S7, Supporting Information) to obtain an expected  $\alpha$  for each  $s$  (solid lines). (c) The sheet kinetic inductance ( $L_{k/\square}$ ) extracted from each resonator, as a function of  $t$ , lies on a curve that is well-described by a single magnetic penetration depth  $\lambda = 1.78 \pm 0.02 \mu\text{m}$  (solid line). The uncertainty in  $\lambda$  represents the s.e. estimated from the covariance matrix of the fit. The  $L_{k/\square}$  saturates to 2.2  $\text{pH}/\square$  in the bulk limit (dashed line).

echo coherence time ( $T_{2,E}$ ) of  $(601 \pm 19) \mu\text{s}$  (Figure 1f), and Ramsey coherence time ( $T_{2,R}$ ) of  $(408 \pm 15) \mu\text{s}$  (Section S4, Supporting Information). We acquire  $T_1$  and  $T_{2,E}$  measurements over 2–5 days for each qubit. Across 11 qubits, the mean time-averaged relaxation time is  $(264 \pm 165) \mu\text{s}$  and the mean time-averaged Hahn echo coherence time is  $(214 \pm 80) \mu\text{s}$ , with 4 qubits attaining nearly lifetime-limited coherence,  $\overline{T}_{2,E} \sim 2\overline{T}_1$  (Figure 1g).

To investigate the material loss channels limiting qubit performance, we measure microwave losses in coplanar waveguide (CPW) and lumped-element (LE) resonators made from  $\beta$ -Ta films (Section S5, Supporting Information), following the methodology developed in Reference [23]. We measure the resonance frequencies ( $f_r$ ) of the resonators to be lower than their simulated  $f_r$ , with CPW resonators displaying particularly large shifts to lower frequencies (Figure 2a). The measured  $f_r$  is extracted from a transmission measurement (Section S6, Supporting Information) and the simulated  $f_r$  is obtained from electromagnetic simulations of the resonator geometry (Section S7, Supporting Information). Modeling this shift to lower frequencies is crucial for identifying resonators during loss measurements and designing qubit wiring layers.

We hypothesize that this shift originates from the kinetic inductance of  $\beta$ -Ta films, which has been reported in previous works [43, 44]. We validate this hypothesis by fabricating 80 CPW resonators with varying gap widths ( $s = 2 - 16 \mu\text{m}$ ) from 11 films with different thicknesses ( $t = 0.02 - 2.00 \mu\text{m}$ ), as kinetic inductance has a distinct dependence on  $s$  and  $t$  [21]. The frequency shift is quantified by  $\alpha = 1 - (f_{r,\text{measured}}/f_{r,\text{simulated}})^2$ , which we interpret as the effective kinetic inductance fraction. Across all CPW resonators,  $\alpha$  increases systematically with decreasing  $s$  and  $t$  (Figure 2b). We model this behavior of  $\alpha$  using a geometric inductance,  $L_g(s)$ , and a kinetic inductance,  $L_k(s, t)$ , acting in series. We use electromagnetic simulations of the resonator surface current distributions to determine  $L_g(s)$  and map the  $L_k(s, t)$  of the resonator to the sheet kinetic inductance of the film,  $L_{k/\square}(t)$  (Section S7, Supporting Information). Resonators fabricated on films with the same thickness yield comparable  $L_{k/\square}(t)$  values (Figure 2c), and the data are well-described by a single curve given by [45, 46]

$$L_{k/\square}(t) = \mu_0 \lambda \coth\left(\frac{t}{\lambda}\right), \quad (1)$$

where  $\mu_0$  is the vacuum magnetic permeability,  $t$  is measured using atomic force microscopy, and  $\lambda$  is the magnetic penetration depth. The fitted  $\lambda$  of  $(1.78 \pm 0.02) \mu\text{m}$  is around 0.1  $\mu\text{m}$  larger than an estimate

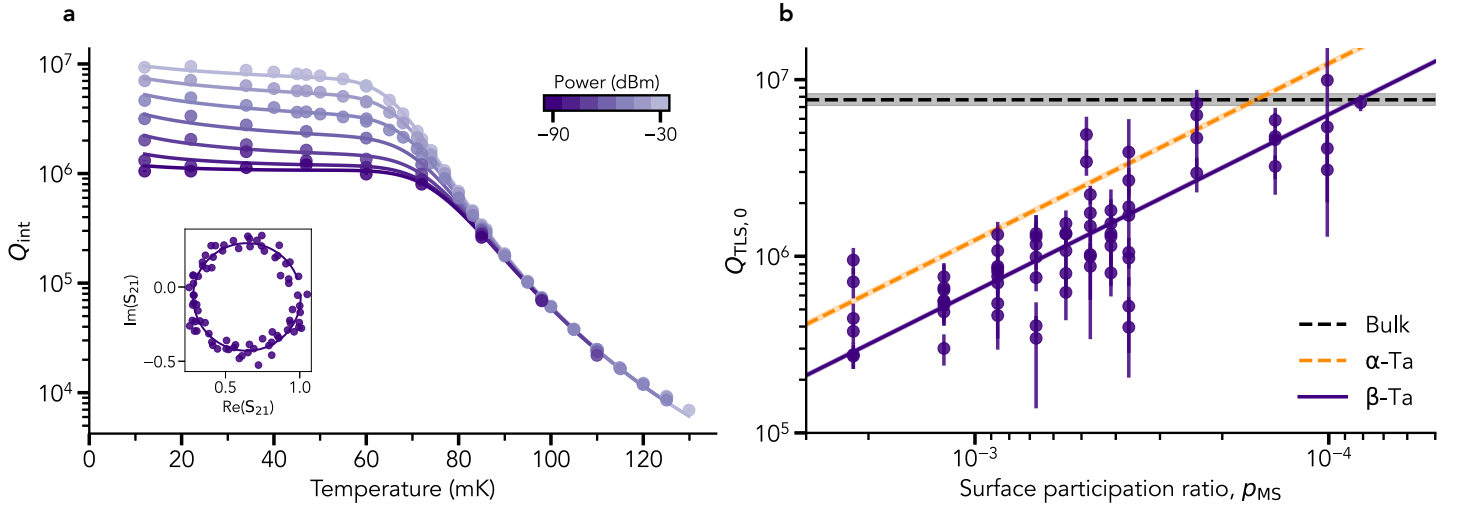


**Figure 3: Quantifying microwave losses in  $\beta$ -Ta resonators.** (a)  $Q_{\text{int}}$  as a function of microwave probe power and mixing chamber stage temperature for a CPW resonator ( $s = 6 \mu\text{m}$ ,  $t = 263 \text{ nm}$ ). Solid lines are fits to a model that parametrizes losses due to TLSs, QPs, and other power- and temperature-independent channels (Section S8, Supporting Information). Inset: Real and imaginary components of the transmission coefficient ( $S_{21}$ ) at a power of  $-90 \text{ dBm}$  and a temperature of  $11 \text{ mK}$ , acquired using a homophasal point distribution [48], and fit to a circle [49] (solid line) to extract  $Q_{\text{int}}$  (Section S6, Supporting Information). Error bars of  $Q_{\text{int}}$  represent the s.e. estimated from the covariance matrix of the circle fit, and are smaller than the data points. (b)  $Q_{\text{TLS},0}$  extracted from power-temperature sweeps of  $Q_{\text{int}}$  for 71  $\beta$ -Ta resonators scales inversely with  $p_{\text{MS}}$ . Error bars of  $Q_{\text{TLS},0}$  represent the s.e. estimated from the covariance matrix of the fit. We choose  $p_{\text{MS}}$  for consistency with previous literature [10, 23, 32]. The data are well-described by a single surface loss tangent (solid line). The loss tangents corresponding to the  $\alpha$ -Ta surface (dashed orange line) and the bulk substrate (dashed black line) and their uncertainties (shaded regions) are taken from Reference [23] for comparison.

calculated assuming the BCS dirty limit (Section S7, Supporting Information). Our approach reliably estimates  $L_{k/\square}$  for thin films ( $t < \lambda$ ) typically used for fabricating superconducting devices. For instance, we expect  $L_{k/\square} \sim 10 - 100 \text{ pH}/\square$  for  $t \sim 400 - 40 \text{ nm}$ .

Superconductors with micron-scale  $\lambda$  values often exhibit increased inductive losses, which may decrease resonator  $Q_{\text{int}}$  [47]. We extract the  $Q_{\text{int}}$  of  $\beta$ -Ta resonators from a transmission measurement (Figure 3a inset; Section S6, Supporting Information), and find that a high  $L_{k/\square}$  coexists with high  $Q_{\text{int}}$ . For instance, a CPW resonator ( $s = 8 \mu\text{m}$ ,  $t = 21 \text{ nm}$ ) fabricated from a film with an  $L_{k/\square}$  of  $(259 \pm 33) \text{ pH}/\square$  exhibits a  $Q_{\text{int}}$  of  $(1.6 \pm 0.1) \times 10^6$  at low powers and temperatures (Section S5, Supporting Information); this is among the highest combinations of  $L_{k/\square}$  and  $Q_{\text{int}}$  reported in the literature [47].

We measure  $Q_{\text{int}}$  at various powers ( $\bar{n}$ ) and temperatures ( $T$ ) to identify the dominant loss channels in  $\beta$ -Ta resonators. Power is expressed as an effective intracavity photon number  $\bar{n}$  after accounting for line attenuation in the measurement chain. A representative CPW resonator (Figure 3a) shows  $Q_{\text{int}}$  ranging from  $10^4 - 10^7$ . At  $T < 50 \text{ mK}$ ,  $Q_{\text{int}}$  decreases with decreasing power; this behavior is consistent with losses due to saturable TLSs [21, 22]. Above  $70 \text{ mK}$ ,  $Q_{\text{int}}$  decreases exponentially with temperature due to the generation of thermal QPs. We fit  $Q_{\text{int}}(\bar{n}, T)$  to a model [23] that separates losses due to TLSs, thermal QPs, and other power- and temperature-independent channels (Section S8, Supporting Information). At the lowest measured power and temperature, TLS losses account for about 98% of total internal losses in the device in Figure 3a. We quantify the TLS loss contribution by  $Q_{\text{TLS},0}$ , a material-dependent fit parameter that constitutes the inverse linear absorption due to TLSs.

We quantify the relative contributions of the surface and bulk TLS baths by studying the dependence of  $Q_{\text{TLS},0}$  on the resonator SPR. In the CPW resonators, the SPR of the metal-substrate interface ( $p_{\text{MS}}$ ) ranges from  $(0.4 - 2) \times 10^{-3}$ , and the LE resonators extend this range to include  $p_{\text{MS}}$  down to  $8 \times 10^{-5}$  (Section S5, Supporting Information). All resonators undergo a post-fabrication buffered oxide etch treatment to reduce the native oxide thickness and remove hydrocarbons associated with fabrication contamination [23, 24]. The  $Q_{\text{TLS},0}$  of 71 CPW and LE resonators increases linearly with decreasing  $p_{\text{MS}}$  (Figure 3b). The linear

dependence indicates that the losses are dominated by surface TLSs across this range of  $p_{\text{MS}}$ , and we do not observe any contribution from bulk TLSs in this range. We extract an effective surface loss tangent ( $\tan \delta$ ) of  $(1.6 \pm 0.1) \times 10^{-3}$ , which is about twice that of  $\alpha$ -Ta reported in Reference [23]. The data are well-explained by a single  $\tan \delta$  regardless of metal film thickness (Section S9, Supporting Information).

We explore potential sources of the higher apparent surface TLS loss compared to  $\alpha$ -Ta in Figure 3b by examining the metal-air (MA) and MS interfaces of the resonators. As the native oxide at the MA interface is a major source of TLSs, we study its composition using X-ray photoelectron spectroscopy (XPS). We fit XPS scans of the Ta4f peaks to extract an effective oxide thickness ( $t_{\text{TaOx}}$ ) of  $(2.9 \pm 0.1)$  nm, which is consistent with cross-sectional STEM images of the MA interface (Section S9, Supporting Information). This value of  $t_{\text{TaOx}}$  is about 1.2 times greater than that for  $\alpha$ -Ta reported in Reference [24]. The increased  $t_{\text{TaOx}}$  can account for 20% of the higher surface losses in  $\beta$ -Ta within a model where MA interface loss scales linearly with the oxide thickness [23] (Section S9, Supporting Information). Such a model assumes a laterally uniform oxide layer. However, scanning electron microscopy images of device sidewalls show protrusions with lateral dimensions of about 100 nm that contribute to increased sidewall roughness (Section S9, Supporting Information). These features can increase the effective oxide volume at the MA interface, and may lead to enhanced surface losses when present in regions with high electric field participation, such as sidewalls [50]. We also acquire cross-sectional STEM images of the MS interface and find a roughly 5 nm-thick amorphous  $\beta$ -Ta layer at the epitaxial interface (Section S9, Supporting Information). This amorphous layer is another potential source of TLS loss, and its loss contribution may be quantified in future work by measuring devices that are designed to independently vary the participation ratios at the MS, MA, and substrate-air interfaces [51, 52, 53].

The  $\tan \delta$  of  $\beta$ -Ta obtained from resonator studies (Figure 3b) allows us to compare qubit performance (Figure 1g) to the linear absorption limit imposed by surface TLSs. The qubits are designed with a  $p_{\text{MS}}$  of  $1.3 \times 10^{-4}$ , which corresponds to an expected  $Q_{\text{TLS},0}$  of 4.8 million based on the extracted  $\tan \delta$ . We note that the distribution of qubit  $\bar{Q}$  exceeds the linear absorption limit; this observation is consistent with qubit operation at powers that saturate TLSs [10, 23].

We observe a large spread in  $\bar{T}_1$  and  $\bar{T}_{2,E}$  across the 11 qubits (Figure 4a). To explain potential reasons underlying this spread, we consider correlations between  $T_1$ ,  $T_{2,E}$ , and other qubit parameters (Section S4, Supporting Information). We find that the qubits with  $\bar{T}_{2,E} < \bar{T}_1$  are also in the offset-charge-sensitive (OCS) regime, as the ratio of their Josephson energy ( $E_J$ ) to their charging energy ( $E_C$ ) ranges from 16 – 28. In contrast, the qubits with  $\bar{T}_{2,E} > \bar{T}_1$  are deep in the transmon regime, with an  $E_J/E_C$  between 74 – 122. By acquiring successive  $T_1$  and  $T_{2,E}$  measurements over a few days (Figure 4b–c), we calculate a time-averaged pure dephasing time ( $\bar{T}_\phi$ ), where the pure dephasing time ( $T_\phi$ ) is obtained using  $T_\phi^{-1} = T_{2,E}^{-1} - 0.5 T_1^{-1}$ . The two groups of qubits exhibit distinct ranges of  $\bar{T}_\phi$ , with  $\bar{T}_\phi$  ranging from 150 to 470  $\mu\text{s}$  in OCS transmons and 500 to 1800  $\mu\text{s}$  in non-OCS transmons (Section S4, Supporting Information). The additional dephasing in the OCS transmons likely arises from charge noise, as charge dispersion increases exponentially with decreasing  $E_J/E_C$  [54].

We note that qubits with lower  $\bar{Q}$  also have higher frequencies (Section S4, Supporting Information), and the qubit with the highest frequency of 5.80 GHz has the lowest  $\bar{Q}$  of  $(1.5 \pm 0.2) \times 10^6$ , suggesting a frequency-dependent qubit quality factor. We rule out relaxation induced by the Purcell effect [55], as our devices incorporate an on-chip Purcell filter and electromagnetic simulations indicate a Purcell-limited  $T_1$  exceeding 5 ms. One possible relaxation channel is radiative coupling to spurious modes of the device package; an electromagnetic simulation of the entire package is needed to verify this possibility [56].

Finally, while we use  $\bar{T}_1$  and  $\bar{T}_{2,E}$  to benchmark qubit performance, the  $T_1$  and  $T_{2,E}$  distributions for some qubits exhibit strongly non-Gaussian features (Figure 4a). These features indicate temporal fluctuations in  $T_1$  and  $T_{2,E}$ , which likely arise from spectral diffusion of strongly-coupled TLSs within the qubit’s frequency neighborhood [57, 58]. The presence of such non-Gaussian features suggests that the mean and standard deviation of the  $T_1$  and  $T_{2,E}$  time series may not faithfully represent the variability in qubit performance, and highlights the need for more detailed statistical analysis to benchmark  $T_1$  and  $T_{2,E}$  fluctuations.

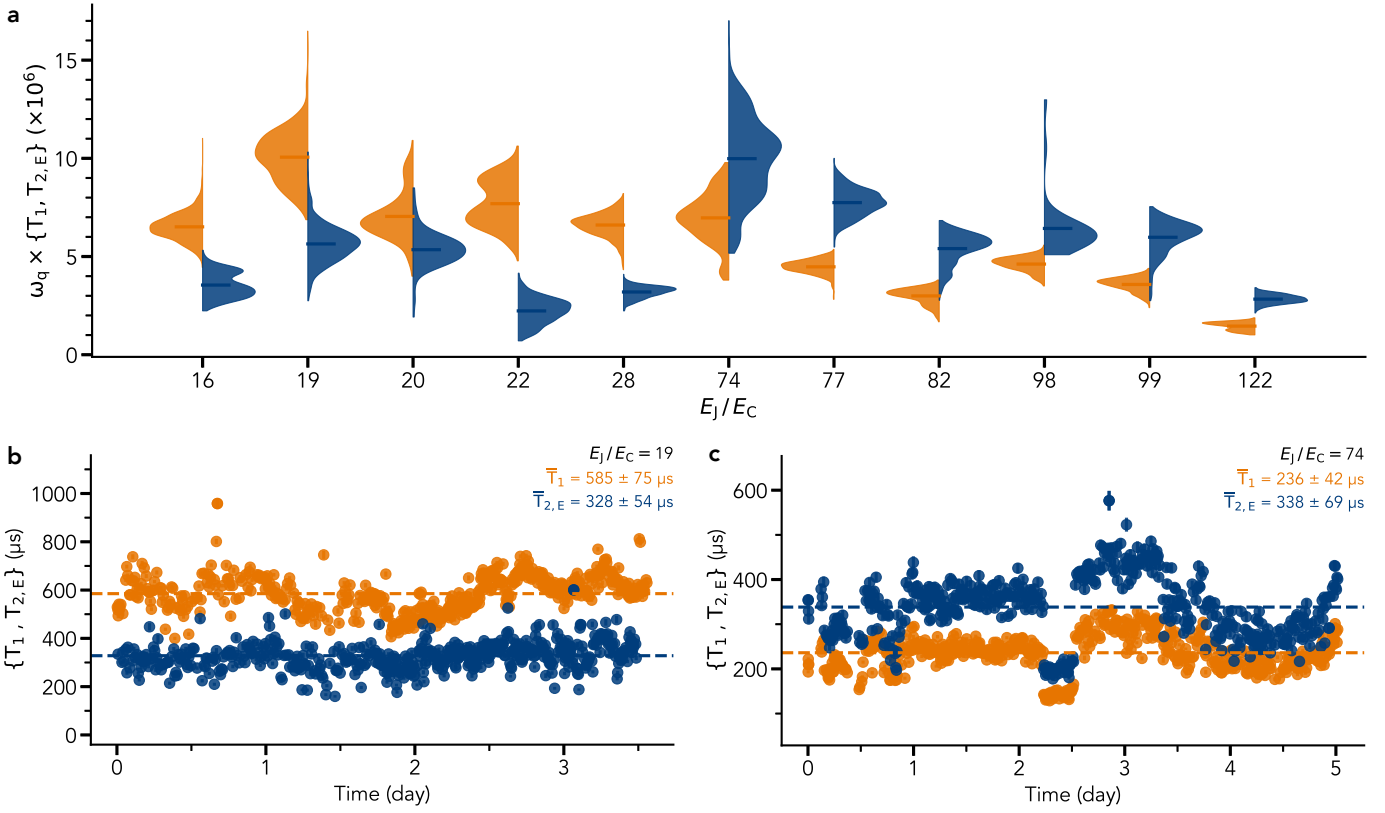


**Figure 4: Performance of  $\beta$ -Ta transmon qubits.** (a) Split violin plot showing the distribution of all  $T_1$  (left, orange) and  $T_{2,E}$  (right, blue) measurement results multiplied by  $\omega_q$  for all 11 qubits ordered by increasing  $E_J/E_C$ . The  $\bar{T}_1$  and  $\bar{T}_{2,E}$  values multiplied by  $\omega_q$  are depicted by horizontal lines within each distribution. The distributions are generated by applying Gaussian kernel density estimation to the sampled data. Results of successive  $T_1$  (orange) and  $T_{2,E}$  (blue) measurements over a few days acquired on (b) an OCS transmon ( $f_q = 2.74$  GHz) with  $E_J/E_C = 19$  and (c) a non-OCS transmon ( $f_q = 4.70$  GHz) with  $E_J/E_C = 74$ . The dashed horizontal lines in (b) and (c) depict the  $\bar{T}_1$  (orange) and  $\bar{T}_{2,E}$  (blue) of each qubit. Error bars of  $T_1$  and  $T_{2,E}$  represent the s.e. estimated from the covariance matrix of the fit, while uncertainties of  $\bar{T}_1$  and  $\bar{T}_{2,E}$  are the s.d. of the time series. Both qubits were measured in the same dilution refrigerator with an identical measurement chain during separate cooldowns (Section S3, Supporting Information).

Further improvements to the performance of  $\beta$ -Ta transmon qubits may be achieved by replacing the sapphire substrate with high-purity silicon, as has been recently demonstrated for  $\alpha$ -Ta [10]. We deposit  $\beta$ -Ta films at room temperature on an intrinsic silicon substrate that is first stripped of its native oxide layer. However, preliminary measurements on CPW resonators fabricated from these films reveal power- and temperature-independent losses that limit  $Q_{\text{int}}$  to  $< 3$  million across 7 resonators, independent of geometry (Section S10, Supporting Information). Identifying the precise source of this loss requires further careful investigation; one plausible candidate is non-saturable dielectric loss originating from the MS interface [59, 60], whose structure differs from that of the  $\alpha$ -Ta-silicon interface.

This work establishes  $\beta$ -Ta on sapphire as a material platform for realizing low-loss superconducting quantum devices. The ability to deposit  $\beta$ -Ta at room temperature makes it a favorable material for industrial-scale Ta qubit fabrication [61]. The large kinetic inductance contribution of  $\beta$ -Ta allows resonators and transmission lines to attain a given frequency at reduced lengths, enabling more compact qubit wiring layouts. Our findings also imply that the presence of minority  $\beta$ -Ta in  $\alpha$ -Ta films may not be as detrimental to superconducting circuit performance as previously assumed, and thus, the stringent requirement of depositing “phase-pure  $\alpha$ -Ta” can be relaxed. Beyond transmon qubits, the coexistence of high kinetic inductance and high quality factor makes  $\beta$ -Ta an attractive material for microwave kinetic inductance detectors [43, 62, 63, 64]. Furthermore, the superconducting gap difference between  $\beta$ -Ta and other metals such as Al, Nb, or  $\alpha$ -Ta can be leveraged to realize on-chip QP traps [65] that protect qubits from relaxation events due to the sudden generation of non-equilibrium QPs [66, 67].

## Conflict of Interest

Nathalie P. de Leon, Princeton University professor, is also a visiting faculty researcher with Google Quantum AI. As a result of her income from Google, Princeton University has a management plan in place to mitigate a potential conflict of interest that could affect the design, conduct, and reporting of this research. Her academic group also has a sponsored research contract with Google Quantum AI. Andrew A. Houck, Princeton University professor, is also a consultant for Quantum Circuits, Inc. (QCI). As a result of his income from QCI, Princeton University has a management plan in place to mitigate a potential conflict of interest that could affect the design, conduct, and reporting of this research.

## Acknowledgments

The authors thank Basil M. Smitham and Saptarshi Chaudhuri for helpful conversations. The authors acknowledge Alexander C. Pakpour-Tabrizi for assisting with qubit fabrication, Ray D. Chang for film growth, and Ambrose Yang and Matthew S. Ai for qubit measurements. This work is primarily supported by the Air Force Office of Scientific Research under award number FA9550-25-1-0172. Some materials characterization is supported by the U.S. Department of Energy, Office of Science, National Quantum Information Science Research Centers, Co-design Center for Quantum Advantage (C2QA) under Contract No. DE-SC0012704. This work was performed in part at the Micro/Nano Fabrication Center (MNFC), a core shared-use facility of the Princeton Materials Institute (PMI). The authors acknowledge the use of Princeton’s Imaging and Analysis Center (IAC), which is partially supported by the Princeton Center for Complex Materials (PCCM), a National Science Foundation (NSF) Materials Research Science and Engineering Center (MRSEC; DMR-2011750). The authors acknowledge MIT Lincoln Labs for supplying a traveling-wave parametric amplifier.

## Data Availability Statement

Data and code associated with this study are available from the corresponding author upon request.

## References

- [1] V. V. Sivak, A. Eickbusch, B. Royer, et al., *Nature* **2023**, *616* 50–55, <https://doi.org/10.1038/s41586-023-05782-6>.
- [2] Z. Ni, S. Li, X. Deng, et al., *Nature* **2023**, *616* 56–60, <https://doi.org/10.1038/s41586-023-05784-4>.
- [3] Google Quantum AI and collaborators, *Nature* **2025**, *638* 920–926, <https://doi.org/10.1038/s41586-024-08449-y>.
- [4] H. Putterman, K. Noh, C. T. Hann, et al., *Nature* **2025**, *638* 927–934, <https://doi.org/10.1038/s41586-025-08642-7>.
- [5] Y. Kim, A. Eddins, S. Anand, et al., *Nature* **2023**, *618* 500–505, <https://doi.org/10.1038/s41586-023-06096-3>.
- [6] T. I. Andersen, N. Astrakhantsev, A. H. Karamlou, et al., *Nature* **2025**, *638* 79–85, <https://doi.org/10.1038/s41586-024-08460-3>.
- [7] Google Quantum AI and Collaborators, *Nature* **2025**, *646* 825–830, <https://doi.org/10.1038/s41586-025-09526-6>.
- [8] Z. H. Liu, Y. Liu, G. H. Liang, et al., *Nature* **2026**, *650* 79–85, <https://doi.org/10.1038/s41586-025-09977-x>.
- [9] N. de Leon, *Nat Phys* **2025**, *21* 1500–1503, <https://doi.org/10.1038/s41567-025-03044-y>.

- [10] M. P. Bland, F. Bahrami, J. G. C. Martinez, et al., *Nature* **2025**, *647* 343–348, <https://doi.org/10.1038/s41586-025-09687-4>.
- [11] H. Deng, Z. Song, R. Gao, et al., *Phys Rev Applied* **2023**, *19* 024013, <https://doi.org/10.1103/PhysRevApplied.19.024013>.
- [12] J. Biznárová, A. Osman, E. Rehnman, et al., *npj Quantum Inf* **2024**, *10* 78, <https://doi.org/10.1038/s41534-024-00868-z>.
- [13] M. Tuokkola, Y. Sunada, H. Kivijärvi, et al., *Nat Commun* **2025**, *16* 5421, <https://doi.org/10.1038/s41467-025-61126-0>.
- [14] S. Ganjam, Y. Wang, Y. Lu, et al., *Nat Commun* **2024**, *15* 3687, <https://doi.org/10.1038/s41467-024-47857-6>.
- [15] A. P. M. Place, L. V. H. Rodgers, P. Mundada, et al., *Nat Commun* **2021**, *12* 1779, <https://doi.org/10.1038/s41467-021-22030-5>.
- [16] C. Wang, X. Li, H. Xu, et al., *npj Quantum Inf* **2022**, *8* 3, <https://doi.org/10.1038/s41534-021-00510-2>.
- [17] M. W. Olszewski, L. Kong, S. Reinhardt, et al., *arXiv preprint* **2026**, <https://doi.org/10.48550/arXiv.2601.20091>.
- [18] K. Bu, Z. Zong, Z. Zhang, et al., *Supercond Sci Technol* **2025**, *38* 035010, <https://doi.org/10.1088/1361-6668/adaaa8>.
- [19] M. H. Read, C. Altman, *Appl Phys Lett* **1965**, *7* 51–52, <https://doi.org/10.1063/1.1754294>.
- [20] L. Glazman, G. Catelani, *SciPost Phys Lect Notes* **2021**, *31*, <https://doi.org/10.21468/SciPostPhysLectNotes.31>.
- [21] J. Gao, Ph.D. thesis, California Institute of Technology, **2008**, ISBN: 978-1-267-59387-0.
- [22] C. Müller, J. H. Cole, J. Lisenfeld, *Rep Prog Phys* **2019**, *82* 124501, <https://doi.org/10.1088/1361-6633/ab3a7e>.
- [23] K. D. Crowley, R. A. McLellan, A. Dutta, *Phys Rev X* **2023**, *13* 041005, <https://doi.org/10.1103/PhysRevX.13.041005>.
- [24] R. A. McLellan, A. Dutta, C. Zhou, et al., *Adv Sci* **2023**, *10* 2300921, <https://doi.org/10.1002/advs.202300921>.
- [25] J. S. Oh, R. Zaman, A. A. Murthy, et al., *ACS Nano* **2024**, *18*, 30 19732–19741, <https://doi.org/10.1021/acsnano.4c05251>.
- [26] J. F. Whitacre, S. M. Yalisove, J. C. Bilello, *J Vac Sci Technol A* **2001**, *19*, 6 2910–2919, <https://doi.org/10.1116/1.1414119>.
- [27] M. Singer, B. Schoof, H. Gupta, et al., In *2024 IEEE International Conference on Quantum Computing and Engineering (QCE)*, volume 01. IEEE, **2024** 1197–1202, <https://doi.org/10.1109/QCE60285.2024.00141>.
- [28] Y. Urade, K. Yakushiki, M. Tsujimoto, et al., *APL Mater* **2024**, *12* 021132, <https://doi.org/10.1063/5.0165137>.
- [29] N. Arlt, K. Houska, J. Braumüller, et al., *arXiv preprint* **2025**, <https://doi.org/10.48550/arXiv.2508.09577>.
- [30] R. Dhundhwal, H. Duan, L. Brauch, et al., *Appl Phys Lett* **2025**, *127* 214005, <https://doi.org/10.1063/5.0302324>.

- [31] A. P. McFadden, T. F. Q. Larson, S. Gill, et al., *Phys Rev Materials* **2025**, *9* 096201, <https://doi.org/10.1103/lwn1-fznb>.
- [32] C. Wang, C. Axline, Y. Y. Gao, et al., *Appl Phys Lett* **2015**, *107* 162601, <https://doi.org/10.1063/1.4934486>.
- [33] M. Bal, A. A. Murthy, S. Zhu, et al., *npj Quantum Inf* **2024**, *10* 43, <https://doi.org/10.1038/s41534-024-00840-x>.
- [34] R. T. Gordon, C. E. Murray, C. Kurter, et al., *Appl Phys Lett* **2022**, *120* 074002, <https://doi.org/10.1063/5.0078785>.
- [35] S. Kono, J. Pan, M. Chegnizadeh, et al., *Nat Commun* **2024**, *15* 3950, <https://doi.org/10.1038/s41467-024-48230-3>.
- [36] P. N. Baker, *Thin Solid Films* **1972**, *14*, 1 3–25, [https://doi.org/10.1016/0040-6090\(72\)90365-3](https://doi.org/10.1016/0040-6090(72)90365-3).
- [37] F. Bahrami, M. P. Bland, N. Shumiya, et al., *Phys Rev B* **2026**, *113* 054505, <https://doi.org/10.1103/4ny9-9n5b>.
- [38] N. Schwartz, W. A. Reed, P. Polash, et al., *Thin Solid Films* **1972**, *14*, 2 333–346, [https://doi.org/10.1016/0040-6090\(72\)90433-6](https://doi.org/10.1016/0040-6090(72)90433-6).
- [39] D. W. Face, D. E. Prober, *J Vac Sci Technol A* **1987**, *5* 3408–3411, <https://doi.org/10.1116/1.574203>.
- [40] D. P. Lozano, M. Mongillo, X. Piao, et al., *Mater Quantum Technol* **2024**, *4* 025801, <https://doi.org/10.1088/2633-4356/ad4b8c>.
- [41] G. Marcaud, D. Perello, C. Chen, et al., *Commun Mater* **2025**, *6* 182, <https://doi.org/10.1038/s43246-025-00897-x>.
- [42] T. A. J. van Schijndel, A. P. McFadden, A. N. Engel, et al., *Phys Rev Applied* **2025**, *23* 034025, <https://doi.org/10.1103/PhysRevApplied.23.034025>.
- [43] K. Kouwenhoven, D. Fan, E. Biancalani, et al., *Phys Rev Applied* **2023**, *19* 034007, <https://doi.org/10.1103/PhysRevApplied.19.034007>.
- [44] S. A. H. de Rooij, R. Fermin, K. Kouwenhoven, et al., *Nat Commun* **2025**, *16* 8465, <https://doi.org/10.1038/s41467-025-63321-5>.
- [45] N. Klein, H. Chaloupka, G. Müller, et al., *J Appl Phys* **1990**, *67* 6940–6945, <https://doi.org/10.1063/1.345037>.
- [46] D. López-Núñez, A. Torras-Coloma, Q. Portell-Montserrat, et al., *Supercond Sci Technol* **2025**, *38* 095004, <https://doi.org/10.1088/1361-6668/adf360>.
- [47] T. Charpentier, A. Khvalyuk, L. Ioffe, et al., *arXiv preprint* **2025**, <https://doi.org/10.48550/arXiv.2507.08953>.
- [48] P. G. Baity, C. Maclean, V. Seferai, et al., *Phys Rev Research* **2024**, *6* 013329, <https://doi.org/10.1103/PhysRevResearch.6.013329>.
- [49] S. Probst, F. Song, P. A. Bushev, A. V. Ustinov, M. Weides, *Rev Sci Instrum* **2015**, *86* 024706, <https://doi.org/10.1063/1.4907935>.
- [50] R. D. Chang, N. Shumiya, R. A. McLellan, et al., *Phys Rev Lett* **2025**, *134* 097001, <https://doi.org/10.1103/PhysRevLett.134.097001>.
- [51] W. Woods, G. Calusine, A. Melville, et al., *Phys Rev Applied* **2019**, *12* 014012, <https://doi.org/10.1103/PhysRevApplied.12.014012>.

- [52] M. Zemlicka, E. Redchenko, M. Peruzzo, et al., *Phys Rev Applied* **2023**, *20* 044054, <https://doi.org/10.1103/PhysRevApplied.20.044054>.
- [53] C. U. Lei, S. Ganjam, L. Krayzman, et al., *Phys Rev Applied* **2023**, *20* 024045, <https://doi.org/10.1103/PhysRevApplied.20.024045>.
- [54] J. Koch, T. M. Yu, J. Gambetta, et al., *Phys Rev A* **2007**, *76* 042319, <https://doi.org/10.1103/PhysRevA.76.042319>.
- [55] A. A. Houck, J. A. Schreier, B. R. Johnson, et al., *Phys Rev Lett* **2008**, *101* 080502, <https://doi.org/10.1103/PhysRevLett.101.080502>.
- [56] W. Dai, S. Hazra, D. K. Weiss, et al., *Phys Rev X* **2026**, *16* 011011, <https://doi.org/10.1103/zdpg-mhpc>.
- [57] P. V. Klimov, J. Kelly, Z. Chen, et al., *Phys Rev Lett* **2018**, *121* 090502, <https://doi.org/10.1103/PhysRevLett.121.090502>.
- [58] M. Carroll, S. Rosenblatt, P. Jurcevic, et al., *npj Quantum Inf* **2022**, *8* 132, <https://doi.org/10.1038/s41534-022-00643-y>.
- [59] M. Scigliuzzo, L. E. Bruhat, A. Bengtsson, et al., *New J Phys* **2020**, *22* 053027, <https://doi.org/10.1088/1367-2630/ab8044>.
- [60] H. Zhou, E. Li, K. Godeneli, et al., *Nat Commun* **2026**, *17* 377, <https://doi.org/10.1038/s41467-025-67066-z>.
- [61] J. Van Damme, S. Massar, R. Acharya, et al., *Nature* **2024**, *634* 74–79, <https://doi.org/10.1038/s41586-024-07941-9>.
- [62] P. Day, H. LeDuc, B. Mazin, et al., *Nature* **2003**, *425* 817, <https://doi.org/10.1038/nature02037>.
- [63] B. A. Mazin, In *Handbook of Superconductivity*, 756–765. CRC Press, **2022**, <https://doi.org/10.1201/9781003139638>.
- [64] T. Chi, L. Shi, R. Su, et al., *Appl Phys Lett* **2024**, *125* 202602, <https://doi.org/10.1063/5.0230767>.
- [65] R. P. Riwar, G. Catelani, *Phys Rev B* **2019**, *100* 144514, <https://doi.org/10.1103/PhysRevB.100.144514>.
- [66] M. McEwen, K. C. Miao, J. Atalaya, et al., *Phys Rev Lett* **2024**, *133* 240601, <https://doi.org/10.1103/PhysRevLett.133.240601>.
- [67] V. D. Kurilovich, G. Roberts, L. S. Martin, et al., *arXiv preprint* **2025**, <https://doi.org/10.48550/arXiv.2506.18228>.